2003

The front on the Northern Flank of Georges Bank in spring: 2. Cross-frontal fluxes and mixing

David S. Ullman
University of Rhode Island

Andrew C. Dale

See next page for additional authors

Citation/Publisher Attribution
Ullman, D. S., A. C. Dale, D. Hebert, and J. A. Barth (2003), The front on the Northern Flank of Georges Bank in spring: 2. Cross-frontal fluxes and mixing, *J. Geophys. Res.*, 108, 8010, doi: 10.1029/2002JC001328, C11. Available at: https://doi.org/10.1029/2002JC001328

The front on the Northern Flank of Georges Bank in spring: 2. Cross-frontal fluxes and mixing

David S. Ullman,[1] Andrew C. Dale,[2] Dave Hebert,[1] and John A. Barth[2]

Received 29 January 2002; revised 25 March 2003; accepted 10 April 2003; published 3 September 2003.

[1] Hydrographic observations made with an undulating vehicle carrying a CTD and concurrent shipboard ADCP velocity observations over a 12-day period are combined to investigate vertical mixing and cross-frontal fluxes on the Northern Flank of Georges Bank. The CTD density time series is analyzed to detect the presence of vertical overturns, the statistics of which are used to infer vertical mixing parameters. Vertical turbulent buoyancy fluxes are downward and most intense, reaching values of 5×10^{-7} W/kg, near the bottom at the edge of the bank and decrease both on- and off-bank. Horizontal, cross-bank buoyancy fluxes are partitioned into mean, tidal pumping, and nontidal eddy components and are computed as a function of cross-isobath/vertical position by averaging in the along-isobath direction. The tidal pumping component is dominant over most of the cross-bank section with a peak value of $\sim 1 \times 10^{-4}$ W/kg, directed off-bank near the bank edge. A diagnosed tidal vertical velocity field is used with mean buoyancy gradients to compute the along-isopycnal skew flux. The horizontal component of this skew flux has similar spatial structure and magnitude to that of the observed tidal pumping flux. The divergent component of the skew flux, at depths above the bottom boundary layer, appears to be convergent north of the bank edge and divergent at the bank edge, suggesting that tidally driven advective processes drive buoyant bank water downward and off-bank at mid-depth and force the upwelling of deep, dense water near the bottom at the bank edge. *INDEX TERMS:* 4528 Oceanography: Physical: Fronts and jets; 4568 Oceanography: Physical: Turbulence, diffusion, and mixing processes; 4560 Oceanography: Physical: Surface waves and tides (1255); 4544 Oceanography: Physical: Internal and inertial waves; *KEYWORDS:* Georges Bank, tidal mixing front, GLOBEC, internal tide, skew eddy flux, turbulent mixing

Citation: Ullman, D. S., A. C. Dale, D. Hebert, and J. A. Barth, The front on the Northern Flank of Georges Bank in spring: 2. Cross-frontal fluxes and mixing, *J. Geophys. Res.*, *108*(C11), 8010, doi:10.1029/2002JC001328, 2003.

1. Introduction

[2] Georges Bank, one of the most productive ecosystems on the North American east coast shelf, has been the subject of intense study under the U.S. GLOBEC program. The primary focus of Phase III of this program was the understanding of cross-frontal exchange processes. As part of this effort, in 1999 we participated in two cruises (March–April 1999 on the Northern Flank and June 1999 on the Southern Flank) designed to obtain hydrography, velocity data, and float trajectories in the vicinity of fronts on the bank. A companion paper [*Dale et al.*, 2003] provides a description of the hydrographic and velocity variability observed in 12 days of intensive SeaSoar/ADCP sampling during the early spring cruise to the Northern Flank (see Figure 1). This paper presents the results of an analysis of cross-frontal property transport at the front on the Northern Flank using this data set.

[3] The central part of Georges Bank remains vertically well-mixed throughout the year due to stirring by the vigorous tidal currents [*Garrett et al.*, 1978; *Flagg*, 1987]. Although the deeper portions of the Bank become thermally stratified in late spring and summer, during the early spring period, thermal stratification is absent. At this time, the water column north of the bank is stratified due to salinity, with cool fresher Scotian Shelf Water and Maine Intermediate Water overlying warm and more saline Maine Bottom Water [*Flagg*, 1987]. The front between the well-mixed bank water and the deep saline water intersects the bottom at approximately the bank edge. Substantial intratidal variability in frontal position and shape is evident, however, with a tongue of warm, deep, saline water advected up and onto the bank during the period of on-bank flow [*Dale et al.*, 2003]. With nutrient levels in the deep Maine Bottom Water known to be high relative to bank waters [*Horne et al.*, 1989; *Townsend and Thomas*, 2001], mixing across this frontal boundary may provide an important source of nutrients and biota to the bank ecosystem, as suggested by *Horne et al.* [1989] for the summertime tidal mixing front in this region.

[4] *Garrett and Loder* [1981] considered a number of different mechanisms that can bring about net cross-frontal

[1]Graduate School of Oceanography, University of Rhode Island, Narragansett, Rhode Island, USA.
[2]College of Oceanic and Atmospheric Sciences, Oregon State University, Corvallis, Oregon, USA.

0148-0227/03/2002JC001328

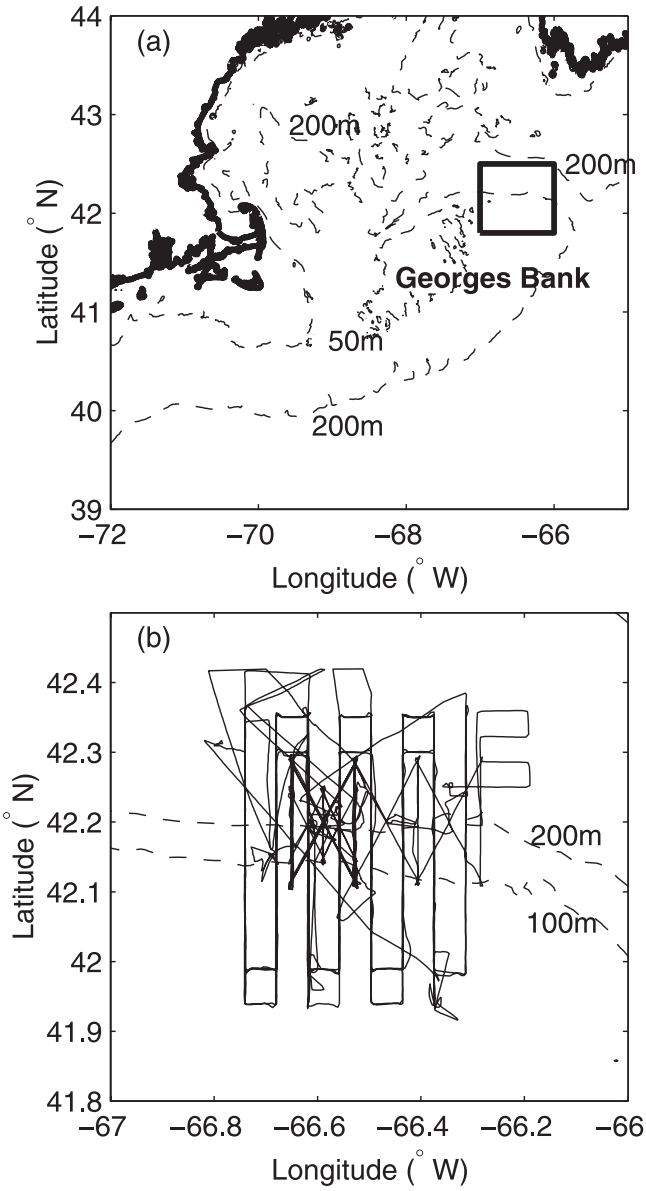

Figure 1. (a) R/V *Oceanus* Cruise 340 survey area on the Northeast Peak of Georges Bank. (b) Ship track over the entire cruise.

flux: mean flow flux, shear dispersion, barotropic eddies, baroclinic eddies, and wind-driven transfer. For Georges Bank, they concluded that frictionally induced mean cross-frontal flow was the dominant mechanism, although this conclusion depended on the assumed (and poorly known) vertical mixing rate. More recently, estimates from moorings of large cross- and along- isobath heat and nutrient eddy fluxes on the Northern Flank [*Marsden*, 1986; *Horne et al.*, 1989] have focused attention on the skew flux concept [*Middleton and Loder*, 1989; *Loder and Horne*, 1991]. A skew eddy flux (a flux in the direction normal to the scalar gradient) arises from interaction of a rotary velocity field with the property gradient and consists of a part due to transport by the Stokes velocity and a non-divergent part that does not affect evolution of scalars. The importance of using the Lagrangian mean velocity to compute fluxes was shown by *Chen and Beardsley* [1998], who found that because of large Stokes velocities, cross-frontal particle exchange over the bank flanks was qualitatively different from what would be inferred from the Eulerian mean fields alone.

[5] Eddy scalar flux estimates from mooring data [*Marsden*, 1986; *Horne et al.*, 1989] are limited in that they do not resolve the spatial structure of the fluxes. Because such estimates may contain a large nondivergent component that is an artifact of the Eulerian nature of the measurement [*Middleton and Loder*, 1989], the actual evolution of the scalar, determined by the flux divergence, can be difficult to interpret. Measurements resolving the spatial structure of the Eulerian eddy flux allow the isolation of the divergent component of the flux, related to the Stokes velocity, and subsequently its divergence.

[6] In this study, we use SeaSoar hydrographic and shipboard ADCP velocity observations, made during a 12-day intensive period, to compute cross-isobath mean and eddy buoyancy fluxes and vertical turbulent fluxes over a cross-bank section. Vertical mixing estimates are derived from an analysis of overturns detected in the density profiles provided by the SeaSoar CTD. The structure and magnitude of the computed cross-isobath eddy fluxes are shown to agree well with that of the skew flux computed from the linearized buoyancy balance and estimates of the tidal period vertical velocity. The divergent component of the skew flux then provides a measure of the true cross-isobath flux.

2. Data and Methods

2.1. Data Sources

[7] The data described here were obtained aboard R/V *Oceanus* on cruise 340 to Georges Bank from March 28 to April 12, 1999. Hydrographic and bio-optical fields were sampled using the towed undulating vehicle SeaSoar equipped with a CTD (SBE 9/11+) with dual temperature and conductivity (T/C) sensors, a fluorometer, and a transmissometer all sampled at 24 Hz. The SeaSoar, towed at 7 knots, profiled from near the surface to approximately 10 m above the bottom, with the maximum attainable depth approximately 120 m. The wavelength of SeaSoar undulations was approximately 1 km in deeper water north of the bank edge and roughly 300 m at the most on-bank locations. The post-processing of the SeaSoar CTD data, including the procedure used to designate the "primary" T/C sensor pair, has been described by *Barth et al.* [2000]. The ship's 150-kHz narrowband ADCP was configured to ensemble average over 150 s using 8-m bins.

2.2. Gridding Procedure

[8] The cruise track covered an approximately 50 km by 50 km area (Figure 1), with the region of heaviest data coverage centered at about the 150-m isobath. The bathymetry in this region is highly two-dimensional. Mean bathymetric gradients in the east-west and north-south directions were computed using a 1-km-resolution bathymetry in the region covered by the surveys (Figure 1b), and the ratio of the mean north-south to the mean east-west gradient magnitude was found to be $\sim$5. The major axes of the tidal

current ellipses are oriented in the approximate cross-isobath (north-south) direction. The uniformity of tidal transport in the cross-isobath direction [*Brown and Moody*, 1987] combined with the strong bathymetric variability produces large cross-isobath tidal current variability. As shown below, the hydrography also varies more strongly in the cross-isobath direction than in the along-isobath direction, suggesting that to lowest order, along-isobath gradients can be neglected.

[9] To focus on processes contributing to cross-frontal fluxes, we collapse the full three-dimensionality of the observations into a single two-dimensional cross-bank section. This allows the construction of pseudo-time series of velocity and hydrography at given vertical and cross-bank locations from observations at different along-bank positions, resulting in increased temporal resolution. The underlying assumption is that the velocity and hydrographic fields vary more strongly in the cross-bank than in the along-bank direction (see *Dale et al.* [2003] for further discussion of this point). The time series resulting from the collapse of dimensionality are used below to compute cross-bank mean and eddy fluxes, and these can be viewed as representing averages over the approximately 50-km along-bank distance covered by the survey.

[10] The underway observations are made in an $\tilde{x}, \tilde{y}, \tilde{z}, \tilde{t}$ coordinate system, where $\tilde{x}$ and $\tilde{y}$ are distances east and north, respectively, $\tilde{z}$ is the vertical coordinate (positive upwards), and $\tilde{t}$ is time. Data locations in the two-dimensional approximation are described in terms of a y, z, t coordinate system, where y is distance north of the bank edge, z is a modified vertical coordinate, and $t = \tilde{t}$. The bank edge is defined as the latitude at which the northward depth gradient is 0.01 and, as described by *Dale et al.* [2003], this latitude varies slightly in the along-bank direction. The vertical coordinate is defined by $z = \tilde{z}\overline{h}/h$ where $h(\tilde{x}, \tilde{y})$ is the local bottom depth and $\overline{h}(y)$ is the mean across-bank depth profile [*Dale et al.*, 2003].

[11] The SeaSoar/ADCP data and the vertical mixing parameters (see below) were averaged onto a grid in this coordinate system with a resolution of Δy = 2 km, Δt = 10 min, and Δz = 8m. At each spatial grid point, the result is a nonuniformly spaced time series over the entire 12-day cruise. The hydrographic variables were observed to vary slowly, on scales long compared to the length of the data set. For this reason, the various time series at each grid point are linearly detrended prior to averaging over the tidal cycle. For the purpose of tidal cycle averaging (described below), we associate each observation time with its particular M_2 tidal phase relative to Greenwich. The observations are generally well distributed over the M_2 tidal cycle, although at the extremes of the cross-bank section, certain phases of the tidal cycle are poorly sampled [*Dale et al.*, 2003].

[12] The validity of the two-dimensional approximation was tested by dividing the data set into eastern and western subdomains. The mean buoyancy field ($\overline{b}(y,z)$) for each subdomain was computed, as described below in section 2.3, and subsequently differenced to provide estimates of along-bank gradients in the mean buoyancy field. These were compared with across-bank gradients computed from the mean buoyancy field derived from the entire data set. Averaged over the cross-section, the mean absolute buoyancy gradient in y was found to be approximately a factor of 5 greater than the mean gradient in the x direction, indicating the validity of the collapse in dimensionality of the data set.

2.3. Averaging Methodology

[13] In this paper, we present tidally averaged cross-bank sections of turbulence, velocity, and buoyancy and its flux derived from the gridded data. To reduce potential bias effects resulting from nonuniform temporal sampling, we average with respect to tidal phase, splitting the tidal cycle into eight M_2 phase intervals (four for turbulence quantities) as described by *Dale et al.* [2003]. We define the phase-mean as the average over the N_m observations within the mth phase bin,

$$\langle a \rangle_m = \frac{1}{N_m} \sum_{n=1}^{N_m} a_{nm}, \tag{1}$$

and the deviation of the phase mean from the overall mean ($\overline{a}$) by $\langle a \rangle'_m = \langle a \rangle_m - \overline{a}$, where the overall mean is the equally weighted average of the M phase means,

$$\overline{a} = \frac{1}{M} \sum_{m=1}^{M} \langle a \rangle_m. \tag{2}$$

We further define the deviation of an instantaneous (gridded) observation from the phase mean by $a'_{nm} = a_{nm} - \langle a \rangle_m$ and expand all variables as

$$a_{nm} = \overline{a} + \langle a \rangle'_m + a'_{nm}. \tag{3}$$

The second term in equation (3) represents tidal fluctuations at the semi-diurnal frequency and its harmonics at quarter-diurnal and sexto-diurnal frequencies, although with eight M_2 phase bins, the latter is poorly resolved. The last term in equation (3) represents variability at other frequencies, for example fluctuations due to high-frequency internal waves generated at the bank edge [*Dale et al.*, 2003] and deviations from the two-dimensional approximation.

[14] Confidence intervals (95% level) for the individual phase means given by equation (1) are estimated using the standard t statistic. The uncertainties in the phase means are then propagated through the computation in equation (2) to generate the uncertainty in the overall mean.

3. Tidal Cycle Variability

[15] To provide perspective for the interpretation of the vertical mixing and tidal flux estimates to be presented below, we first examine the tidal cycle variability in the hydrographic and velocity fields. Sections showing the spatial structure of the density and cross-bank velocity phase mean fields show that strong tidal currents interacting with the topography at the bank edge produce substantial variability in the hydrographic structure over the tidal cycle (Figure 2).

[16] Cross-bank tidal currents are strongest over the bank and weaken rapidly over the sloping bank edge. Vertical phase propagation is also apparent in Figure 2, whereby currents near the bottom at the bank edge lead those higher in the water column and farther on-bank. The velocity field is strongly convergent at the bank edge

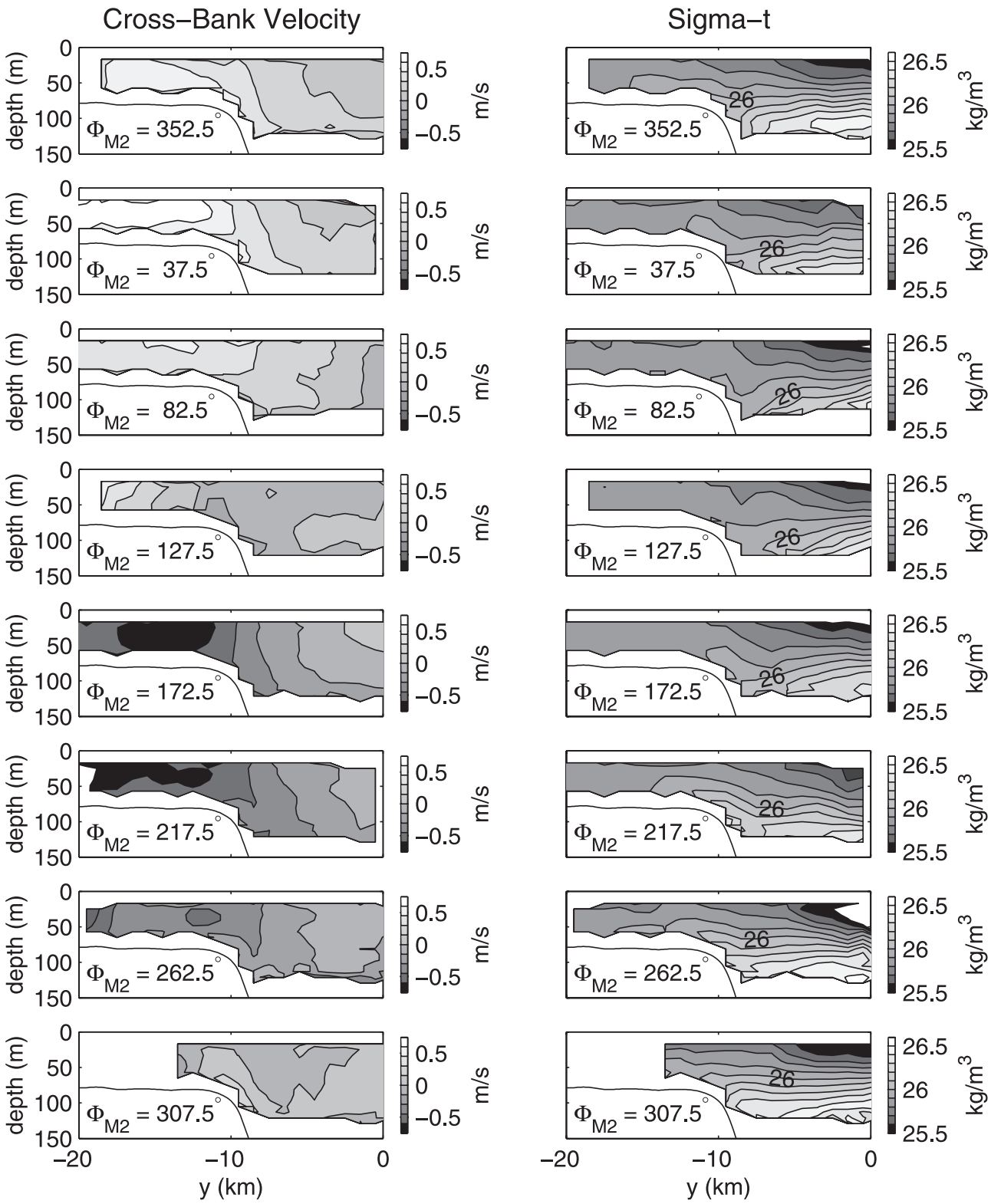

Figure 2. Cross-bank sections of phase mean (left) cross-bank velocity and (right) density for each of eight M_2 phase bins. The center of each 45° phase bin is shown in the lower left of each panel. Maximum off-bank flow occurs approximately in the Φ = 37.5° bin and maximum on-bank flow at Φ = 217.5°.

during off-bank (northward) flow and divergent when the flow is on-bank, with a suggestion that the convergence/divergence is strongest during the period when the flow is accelerating.

[17] The evolution of the density field over the tidal cycle is primarily a response to the strong cross-bank advection. The bottom intersection of the front forming the boundary between bank water and deep Maine Bottom Water (σ_t = 26)

extends farthest on-bank at the end of the on-bank phase of the tidal cycle. A half tidal cycle later, the frontal isopycnals have been driven off-bank. In addition to the response to horizontal advection, significant vertical motion of the isopycnals is evident as well. Careful examination of Figure 2 reveals a slight asymmetry between the responses to on-bank and off-bank flow. Over the bank edge, the pycnocline is lowest in the water column at the end of the off-bank phase of the tide. The pycnocline reaches its highest point, however, roughly during the period of maximum on-bank flow, due to vertical advection arising from the horizontal divergence that is strongest during the accelerating periods of on-bank flow. The resulting non-zero covariance between buoyancy (density) and velocity will be seen later to produce a localized tidal buoyancy flux.

4. Vertical Mixing

[18] Overturning scales were estimated from the full-resolution 24-Hz SeaSoar CTD data using the primary T/C sensor pair. Typically, the analysis of vertical overturns is performed on vertical density profiles [*Thorpe*, 1977; *Dillon*, 1982; *Galbraith and Kelley*, 1996] using sorting techniques introduced by *Thorpe* [1977]. The SeaSoar, however, samples along a sloping path producing a combined vertical-horizontal profile. We perform Thorpe-sorting on individual segments of the SeaSoar density record, as if the profile were vertical, and justify this approach below.

[19] For a density profile measured by an instrument along a sloping trajectory in the presence of internal waves, density inversions not related to mixing could appear if the internal wave slope exceeds the slope of the instrument trajectory. Experiments with breaking internal waves show that under conditions of zero ambient velocity shear, waves are unstable when the ratio of wave height to wave length exceeds approximately 0.1, with the ratio decreasing rapidly in the presence of shear [*Thorpe*, 1978]. Because waves with slope at or above this threshold will be unstable and break, we can expect no internal waves with higher slope to be present. As described below, we limit the overturn analysis to those data segments for which the magnitude of the SeaSoar vertical velocity is greater than 0.25 m/s. For these segments, the mean SeaSoar trajectory slope dz/dx is $\sim$0.3 and approximately 90% of the trajectory slopes are greater than 0.1, indicating that internal waves are unlikely to contribute significantly to the observed density inversions.

[20] Oceanic turbulence is known to occur in patches that are flattened in the vertical dimension, with typical aspect ratios of O(10-100) [*Gregg*, 1987], and direct numerical simulation experiments show that the patches are composed of multiple, interacting overturns [*Smyth et al.*, 2001]. Turbulence in a strong tidal regime such as Georges Bank is forced by shear instability [*Burgett et al.*, 2001], and the horizontal scale over which the vertical current shear and the background stratification varies is of the order of the topographic scale, i.e., kilometers. With the turbulent forcing and the stratification expected to be substantially uniform over the horizontal scale sampled during the passage of the SeaSoar through a mixing patch (e.g., for a 10-m-high patch, the horizontal distance traveled is $\leq$ 100 m), the distribution of turbulent overturns will be statistically uniform as well. Therefore the oblique sampling of a turbulent patch should be equivalent to vertical sampling because the multiple overturns encountered in the two cases will be statistically similar. If this were not the case, one would expect to detect a relationship between the computed overturning scale and the trajectory slope. After applying the overturn-detection procedure described below to the entire data set and plotting Thorpe scale versus slope (not shown), we find no such relationship, leading us to believe the validity of overturning scales derived from oblique sampling of the density field.

[21] The first step in the detection of overturns was to identify monotonically ascending and descending sections of the record using a threshold on the minimum allowable SeaSoar vertical velocity of 0.25 dbar/s. To ensure that large overturns were not artificially undersampled, the analysis was further restricted to data segments with a pressure range of at least 20 dbar. The density profile $\rho(z)$ for each segment was then reordered into a gravitationally stable profile $\hat{\rho}(z)$. If a water parcel at depth z_n must be moved to depth z_m to generate the stable profile, the Thorpe displacement (d_m') at depth z_m is defined as $d_m' = z_m - z_n$ [*Thorpe*, 1977]. The corresponding Thorpe fluctuation (ρ_m) is $\rho_m' = \rho(z_m) - \hat{\rho}(z_m)$. We use the *Galbraith and Kelley* [1996] definition of a reordering region as a depth span such that all overlying (underlying) water is of lower (higher) density. The Thorpe scale (L_T), a measure of the size of the overturn, is the root mean square (rms) Thorpe displacement calculated over the entire reordering region [*Thorpe*, 1977]. The corresponding measure of the magnitude of the density inversion is the rms Thorpe fluctuation (ρ_{rms}').

[22] We used the method of *Galbraith and Kelley* [1996] to separate inversions that could be reliably attributed to overturning motions from those that were most likely due to measurement noise. The first test rejects those reordering regions with $L_T < 2\delta z$ and $\rho_{rms}' < 2\ \delta\rho$, where $\delta z = 0.17$ dbar and $\delta\rho = 0.0006$ kg/m^3 are the estimated instrument resolutions for pressure and density. The remaining reordering regions are then examined using a run-length test. With a "run" defined as a number of adjacent values of one sign in the Thorpe fluctuation series, the rms length of runs within each reordering region is computed and compared with a cutoff value separating runs that are likely due to noise from those that are potentially signatures of overturns. Reordering regions for which the rms run length is less than this cutoff value are rejected as noise. The cutoff run length was empirically determined as the run length for which the run length probability density function (PDF) for a representative section of data was double the theoretical noise PDF [*Galbraith and Kelley*, 1996]. We estimated a value of 6 as the cutoff run length, using this method. The final step discards reordering regions caused by systematic CTD errors, measured by the deviation from linearity of the T-S relation within the region (using the cutoff values of *Galbraith and Kelley* [1996]).

[23] This procedure was applied to all SeaSoar CTD data, resulting in a time series of overturn parameters along the shiptrack. Figure 3 shows a typical cross-bank density section with the overturns indicated as vertical lines of length equal to the Thorpe scale. In this example, large overturns are observed over the bank where stratification is weak, with overturns becoming smaller as the bank edge is

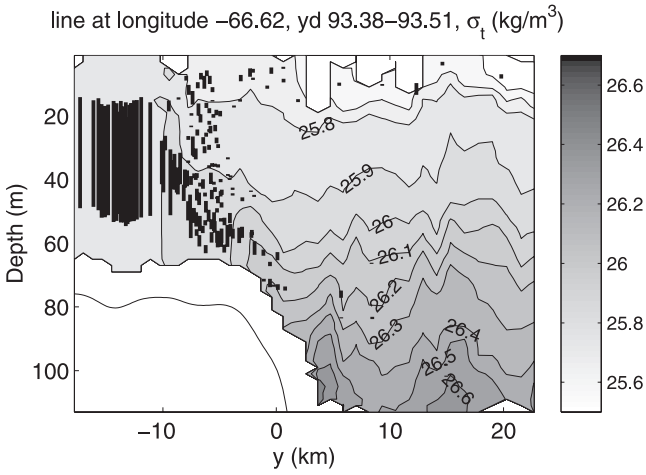

Figure 3. Cross-bank density section during the late stage of on-bank flow (Φ = 216–306°). The vertical lines are significant overturns with the length of the line equal to the Thorpe scale for the particular overturn.

approached. Except for a few scattered overturns in the surface layer, near the edge of the bank, overturns are confined to a near-bottom region that appears to coincide with a tongue of dense water that has been advected up onto the bank. Although the pattern of overturning scales seen in Figure 3 is fairly typical, the use of the threshold on Thorpe fluctuation discussed above often results in the rejection of overturns in the well-mixed region on the bank. This should be borne in mind when interpreting the average sections shown below, in that this will result in an underestimation of Thorpe scales in the well-mixed region.

[24] The gradient Richardson number (*Ri*) was calculated from the ADCP velocity shear and the buoyancy frequency estimated from the SeaSoar CTD. Reordered density profiles were averaged in time over the ADCP ensemble time (150 s) and spatially using a triangular window with half-width equal to the ADCP bin size (8 m). This ensures that buoyancy frequency and shear measure variability at similar scales. Figure 4 shows the PDF for *Ri* estimates computed over the entire cruise. A large fraction of the estimates (~28%) are less than the critical value of 0.25, reflecting the fact that much of the towing occurred within the well-mixed region on the bank. The PDF for estimates at the location and time of an identified overturn (Figure 4) shows that *Ri* less than about 1 are more common at overturns than overall, suggesting a correspondence between overturning signatures and low Richardson number. Note, however, that the PDF of overturning *Ri* decreases below $Ri \approx 0.15$ because overturns cannot be resolved in the very low stratification regimes represented by low *Ri* in this environment.

[25] The experimental finding that $L_T \sim L_O$ [*Dillon*, 1982], where L_O is the Ozmidov scale, allows the estimation of the turbulent dissipation rate,

$$\epsilon = L_O^2 N^3 \sim L_T^2 N^3, \tag{4}$$

where N is the buoyancy frequency computed from the sorted density profile and averaged over individual reordering regions. If the dominant balance in the turbulent energy equation is between shear production, dissipation, and buoyancy flux, then the eddy diffusivity for mass can be written as

$$K_\rho = \frac{R_f}{(1-R_f)}\frac{\epsilon}{N^2} \sim \frac{R_f}{(1-R_f)} L_T^2 N, \tag{5}$$

where R_f is the flux Richardson number, the ratio of the buoyancy flux to the shear production terms [*Osborn*, 1980]. The factor $R_f/(1 - R_f)$ is often referred to as the mixing efficiency and an upper bound on this quantity of 0.2 is often used in practice [*Osborn*, 1980]. However, as argued by *Peters and Bokhorst* [2001], the flux Richardson number cannot be independent of *Ri* when $Ri \rightarrow 0$ which, as was shown above, often occurs on Georges Bank. *Peters and Bokhorst* [2001] determined that use of a constant mixing efficiency in equation (5) results in overestimation of the eddy diffusivity by up to a factor of 10. For this reason we follow *Peters and Bokhorst* [2001] and use the empirical formula, based on laboratory and large-eddy simulation experiments, of *Schumann and Gerz* [1995] to estimate the turbulent Prandtl number $Pr_t = Ri/R_f$ (and thus R_f) from *Ri*,

$$Pr_t = 0.63\exp\left(\frac{-Ri}{0.1197}\right) + \frac{Ri}{0.19}. \tag{6}$$

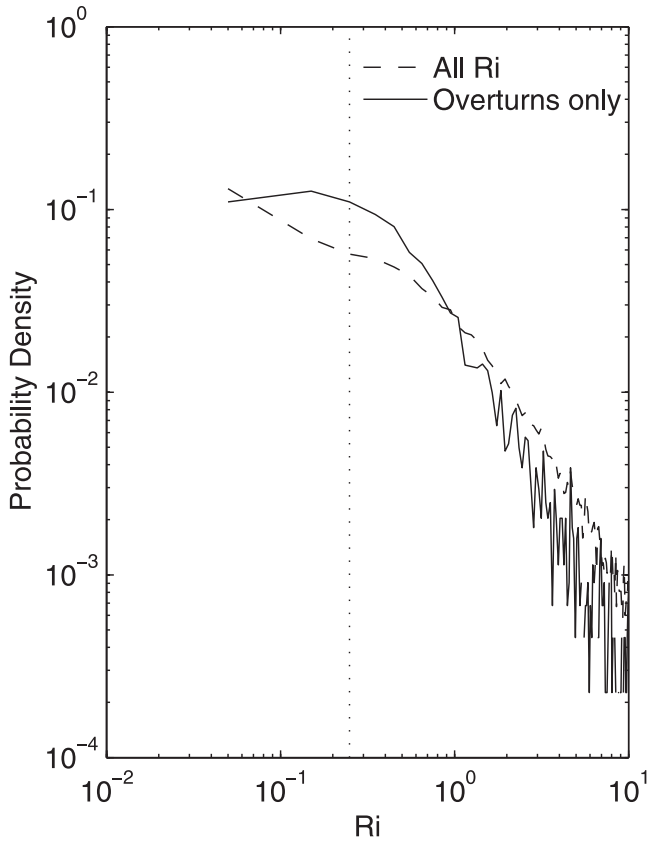

Figure 4. Probability density function for Richardson number. The dashed line is the PDF for all Richardson number estimates and the solid line the PDF for estimates at the time and location of an overturn. The critical Richardson number of 0.25 is indicated by the dotted line.

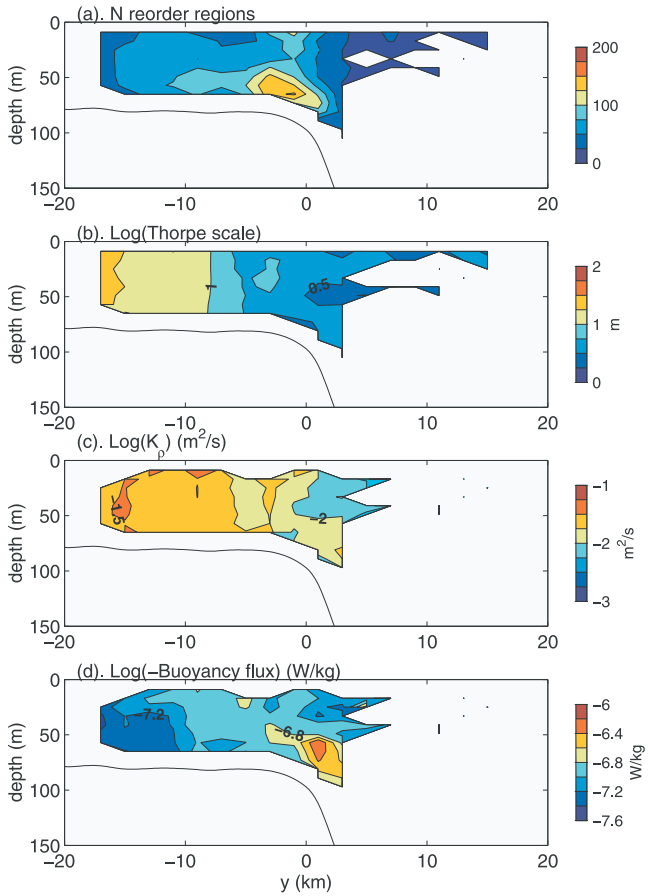

Figure 5. Overall cruise averaged vertical mixing parameters. (a) Number of significant reordering regions. (b) Thorpe scale. (c) Vertical turbulent diffusivity. (d) Vertical turbulent buoyancy flux.

[26] Spatial variability in vertical mixing was investigated by gridding the vertical overturn data using the cross-bank grid, and phase averaging over the M_2 tidal cycle. Four phase bins are used in this procedure, rather than the eight used for velocity and buoyancy, because the sampling density of the episodic turbulence is relatively sparse. A sharp gradient in the number of significant reordering regions is observed at the bank edge (Figure 5a), with essentially no overturns detected in the off-bank region. Overturns are primarily detected in the lower portion of the water column over the bank, with a peak near the bank edge. A secondary peak in the number of overturns is found near the surface at the bank edge. The decrease in the number of overturns near the on-bank extreme of the section is likely due to the inability to detect overturns in the vertically well-mixed conditions prevailing there; recall that the CTD density resolution limits the detection of overturns with weak Thorpe density fluctuations.

[27] Mean Thorpe scales increase in the on-bank direction with values of O(10 m) in the well-mixed zone decreasing to 0.5–1 m in the near-bottom region at the bank edge (Figure 5b). Estimated average vertical turbulent diffusivities (K_ρ) are in the range $1 \times 10^{-3} - 1 \times 10^{-1}$ m^2/s with highest values over the bank and decreasing in the off-bank direction (Figure 5c). Defining a buoyancy anomaly as

$$b = \frac{-g}{\rho_0}(\rho - \rho_0), \tag{7}$$

with ρ_0 a reference density, taken as the overall average value, the vertical turbulent buoyancy flux is

$$F_{turb} = -K_\rho b_z, \tag{8}$$

where the subscript z denotes differentiation. The average vertical turbulent buoyancy flux (Figure 5d) is generally low and downward (O(-1×10^{-7} W/kg)) over the on-bank portion of the section due to the low level of stratification there. Highest turbulent fluxes occur in the lower part of the water column near the bank edge where fluxes of O(-5×10^{-7} W/kg) are observed.

5. Cross-Frontal Flux

[28] With the buoyancy anomaly defined by equation (7), we now consider the scalar evolution equation for buoyancy. Neglecting horizontal diffusion, the buoyancy balance can be written as

$$b_t + (ub)_x + (vb)_y + (wb)_z + (F_{turb})_z = 0, \tag{9}$$

where the subscripts (x, y, z, t) denote differentiation, with x, y, z positive in the along-bank (east), cross-bank (north), and upward directions, respectively. As discussed in section 2.2, mean buoyancy gradients in the cross-bank direction are a factor of 5 greater than along-bank gradients, indicating that in equation (9), the ratio of along-bank advection to cross-bank advection ($u\ b_x$)/($v\ b_y$) is O(0.2). We therefore neglect the along-bank divergence in equation (9), and proceed to examine the resulting two-dimensional buoyancy balance. With the gridded SeaSoar/ADCP observations subsequently used to evaluate the fluxes, a more appropriate view of equation (9) with the second term neglected is as representative of the buoyancy balance averaged over the along-isobath extent of the SeaSoar surveys (~50 km).

[29] If all variables are expanded using equation (3), the subscripts are dropped for clarity, and the equation is averaged over the tidal period, the result is

$$\overline{b}_t + (\overline{v}\overline{b})_y + (\overline{w}\overline{b})_z + \left(\overline{\langle v\rangle'\langle b\rangle'}\right)_y + \left(\overline{\langle w\rangle'\langle b\rangle'}\right)_z + \left(\overline{\langle v'b'\rangle}\right)_y + \left(\overline{\langle w'b'\rangle}\right)_z + \left(\overline{F_{turb}}\right)_z = 0, \tag{10}$$

where the angle brackets and overbar represent, respectively, a tidal phase mean (average over an individual phase bin) and a tidal average. The tidally averaged buoyancy is assumed to vary slowly in time (i.e., over many tidal cycles).

[30] We refer to the terms in equation (10) as mean fluxes (terms 2 and 3) and eddy fluxes (terms 4–7), with the latter composed of tidal pumping fluxes (terms 4 and 5), and nontidal fluxes (terms 6 and 7). This partition of the eddy flux is artificial in the sense that it arises from the particular phase averaging methodology adopted here (see section 2.3); however, it provides for a separation of tidal and nontidal

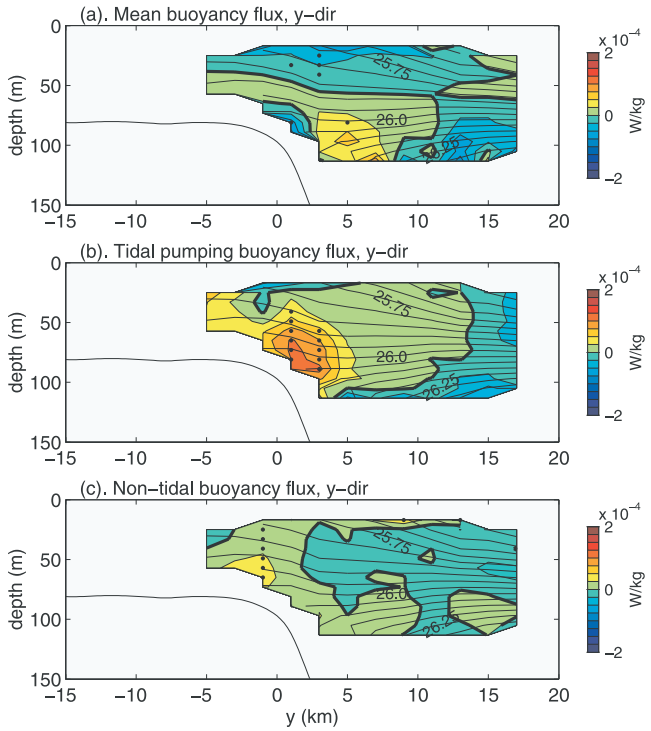

Figure 6. Computed cross-isobath buoyancy fluxes. (a) Mean flux ($\overline{v}\overline{b}$). (b) Tidal pumping flux $\overline{\langle v\rangle'\langle b\rangle'}$. (c) Nontidal flux ($\overline{\langle v'b'\rangle}$). Zero flux contours are drawn as heavy black lines and the mean density field is shown by the thin black lines. The black dots show the locations where the computed flux is significantly different from zero at the 95% level.

effects, with the latter poorly resolved by the observations. The tidal pumping fluxes arise from the covariance between buoyancy and velocity phase means. As the phase means are computed in bins of 45° of M_2 phase, only those frequencies resolved by this sampling (M_2, M_4, and M_6) contribute to this component of the eddy flux. The nontidal fluxes result from covariance between buoyancy and velocity fluctuations at all other frequencies. Note that with the observations sampled over approximately 50 km along-bank, the nontidal flux in the two-dimensional approximation adopted here may also contain a noise contribution due to covariance arising from along-bank variability.

[31] For a sloping front aligned along isobaths as is found in the study area, all of the individual fluxes (terms within parentheses) in equation (10) may represent cross-frontal transports. The cross-isobath (y) terms are calculated from the SeaSoar/ADCP data on the cross-isobath/vertical grid defined above, while the turbulent flux term was estimated in the previous section from the analysis of overturns and was averaged onto the same grid (Figure 5d). The vertical advective fluxes cannot be accurately addressed using the present data set; these terms will be discussed below.

[32] Computed cross-isobath mean ($\overline{v}\overline{b}$), tidal pumping ($\overline{\langle v\rangle'\langle b\rangle'}$), and nontidal ($\overline{\langle v'b'\rangle}$) buoyancy fluxes averaged over the entire cruise are shown in Figure 6. Confidence intervals (95% level) for phase means and overall means are estimated as described in section 2.3, with standard error propagation techniques used to derive confidence intervals on the fluxes. These confidence intervals are used to denote locations (marked with black dots in Figure 6) where flux estimates are significantly different from zero.

[33] Over most of the cross-section, mean cross-bank buoyancy fluxes are not significantly different from zero (Figure 6a). There is a small region in the upper part of the water column in a 5 km region around the bank edge where a weak ($\sim 2.5 \times 10^{-5}$ W/kg) statistically significant negative mean flux occurs, associated with negative (on-bank) mean flow. In the lower part of the water column, there are two isolated grid points where statistically significant mean fluxes also occur. In general, however, mean fluxes are weaker than the peak tidal pumping fluxes (Figure 6b), as was observed on the Northern Flank of Georges Bank by *Marsden* [1986].

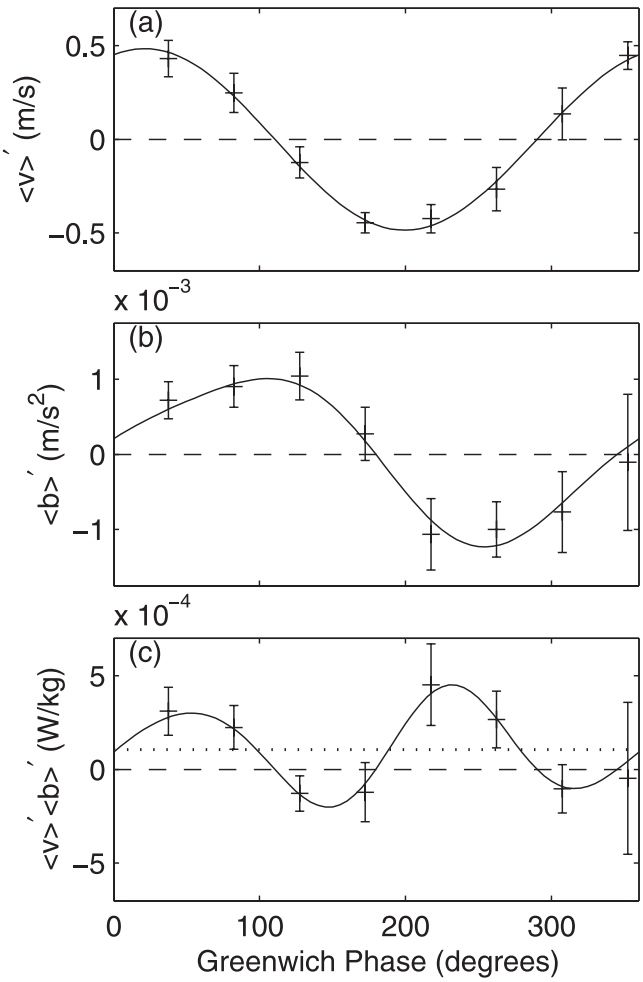

Figure 7. Tidal variation of (a) velocity, (b) buoyancy, and (c) the product of velocity and buoyancy at the cross-bank grid point located at $y = 1$ km, $z = 73$ m. Plotted in Figures 7a and 7b are deviations of phase means from the overall mean and in Figure 7c the product of the velocity and buoyancy phase mean deviations versus M_2 Greenwich phase. The error bars show the 95% confidence limits for the phase means. The solid curves in Figures 7a and 7b are harmonic fits using M_2 and M_4 constituents. The solid curve in Figure 7c is the product of the velocity and buoyancy harmonic fits. The dotted line in Figure 7c shows the overall mean tidal pumping buoyancy flux.

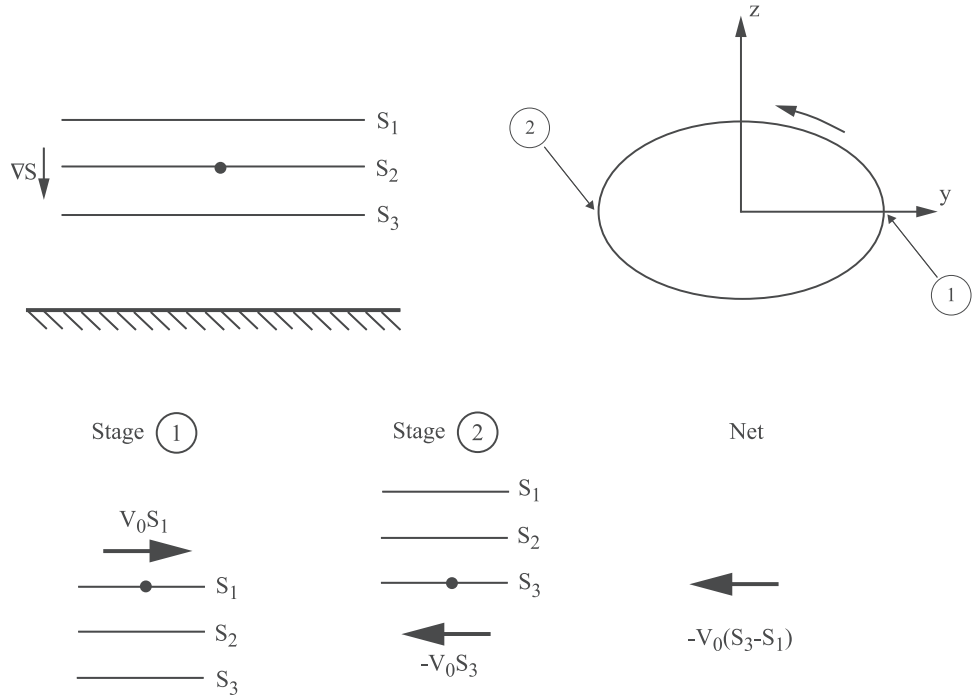

Figure 8. Illustration of a skew eddy salinity flux following Loder and Horne [1991] for the case of rotary motion in the y, z plane acting on a vertical salinity gradient. During tidal stage 1, the instantaneous flux at the indicated point is to the right at a time when the salinity is less than the average salinity ($S_1 < S_2$) because of downward vertical advection over the previous half cycle. One half cycle later, at stage 2, the flux is to the left with the salinity higher than the average salinity ($S_3 > S_2$). The magnitude of the flux at stage 2 is larger than the flux at stage 1, thus producing a net salt flux to the left (normal to the salinity gradient).

[34] Significant off-bank tidal pumping flux, with peak values of O (1×10^{-4} W/kg), occurs in the lower part of the water column in an approximately 5-km region around the break in slope at the bank edge (Figure 6b). This is the location of the mean front between the Maine Bottom Water at depth off-bank and the less dense bank water. It is also the region of highest vertical turbulent buoyancy flux, as inferred from Thorpe sorting (Figure 5d). At depths above about 80 m in the vicinity of the bank edge, mean isopycnals slope downward in the off-bank direction with more buoyant water off-bank (Figure 6). Thus, relative to the mean buoyancy field in this region, the (positive) tidal pumping flux is up-gradient, although without the corresponding vertical flux, this conclusion is tentative. The nontidal eddy flux is much smaller than the tidal pumping term at the bank edge (Figure 6c), and is significantly different from zero only in a small section over the bank itself. The non-zero flux could be due to the effects of the large-amplitude internal waves generated at the bank edge during off-bank flow, which propagate on-bank when the flow subsides, and which ultimately are dissipated over the bank [*Dale et al.*, 2003]. However, with the possibility of a spurious flux arising from along-bank covariability, we can only speculate on this point.

[35] Non-zero tidal pumping fluxes result from correlation between velocity and buoyancy fluctuations. If the tidal variation in buoyancy at a fixed grid point were due only to horizontal tidal advection of a mean horizontal gradient, the buoyancy and velocity fluctuations would be in quadrature with no resulting net flux. Velocity and buoyancy phase mean deviations at the grid point located at $y = 1$ km, $z = 73$ m are shown in Figures 7a and 7b. Note the rapid decrease in buoyancy during the early stages of on-bank flow (negative velocity) and the fact that minimum buoyancy occurs about 50° after maximum on-bank flow. Buoyancy fluctuations are thus phase shifted from the quadrature relationship resulting in a positive (off-bank) tidal pumping buoyancy flux (Figure 7c).

6. Cross-Bank Skew Flux

[36] With the tidal pumping flux clearly the dominant cross-isobath buoyancy flux component in the lower part of the water column over the bank edge, we now examine a simple model for the skew eddy flux [*Middleton and Loder*, 1989]. The spatial structure of the skew flux, estimated using a linear assumption, will be shown to reasonably agree with the computed tidal pumping flux. The skew flux model can then provide a qualitative view of the nontidal, Lagrangian (essentially Stokes) velocity in the y–z plane.

[37] *Loder and Horne* [1991] suggested that eddy scalar fluxes on Georges Bank might, in large part, be skew fluxes directed normal to the scalar gradient [*Middleton and Loder*, 1989]. Skew fluxes arise when a component of the mean scalar gradient lies in the plane of a rotary oscillatory velocity (here taken to be M_2 tidal velocities), and in general can be separated into nondivergent and divergent parts [*Middleton and Loder*, 1989]. Time evolution of scalar

concentration (at timescales long relative to tidal timescales) arises only in response to the divergent component, which is non-zero only in the presence of a non-zero Stokes velocity [*Middleton and Loder*, 1989].

[38] A cross-bank flux can result from the coupling of either rotary motion in the horizontal plane with an along-bank gradient, or rotary motion in the vertical/cross-isobath plane with a vertical gradient. Having neglected along-bank gradients in the present context, the latter combination will be investigated here. A schematic of the flux mechanism in this case is illustrated in Figure 8, adapted from *Loder and Horne* [1991], where we note that in this example, with horizontal homogeneity of currents and stratification, the skew flux is entirely nondivergent as there is no Stokes velocity. In addition to the cross-bank skew flux, the rotary motion in Figure 8, in combination with a cross-bank gradient, produces a vertical skew flux component as well.

[39] To focus on semi-diurnal tidal advection and to simplify the problem, we first neglect the nontidal fluctuations in equation (3) and the nontidal eddy flux in equation (10). Subtracting equation (10) from equation (9) and using the truncated expansions (e.g., $b = \overline{b} + \langle b\rangle'$) gives an equation describing buoyancy fluctuations at tidal periods,

$$\langle b\rangle'_t + \left(\overline{v}\langle b\rangle' + \langle v\rangle'\overline{b} + \langle v\rangle'\langle b\rangle' - \overline{\langle v\rangle'\langle b\rangle'}\right)_y + \left(\overline{w}\langle b\rangle' + \langle w\rangle'\overline{b} + \langle w\rangle'\langle b\rangle' - \overline{\langle w\rangle'\langle b\rangle'}\right)_z + \left(F'_{turb}\right)_z = 0. \quad (11)$$

Expressing the turbulent flux as an eddy diffusion as in equation (8), the ratio of the turbulent flux divergence to the time rate of change term in equation (11) is $K_\rho/(\sigma H_0^2)$, where σ is the tidal frequency and H_0 is a representative water depth. Using a typical value of $K_\rho = 10^{-2}$ m^2/s at the bank edge from Figure 5 c and a depth of 100 m, this ratio is O(5×10^{-2}) for the semidiurnal tide, allowing neglect of vertical mixing in equation (11) outside of the bottom boundary layer. The fluxes in equation (11) arising from mean advection of the tidal buoyancy field (e.g., $\overline{v}\langle b\rangle'$) can be neglected in comparison with those due to tidal advection of the mean buoyancy (e.g., $\langle v\rangle'\overline{b}$) as the ratio of these terms is $\overline{v}/\langle v\rangle'$, which from *Dale et al.* [2003] is O(0.1) or less. In the weakly nonlinear case considered by *Middleton and Loder* [1989], where the tidal excursion is much smaller than topographic or frontal length scales, and neglecting vertical turbulent mixing, equation (11) reduces to

$$\langle b\rangle'_t + \left(\langle v\rangle'\overline{b}\right)_y + \left(\langle w\rangle'\overline{b}\right)_z = \langle b\rangle'_t + \langle v\rangle'\overline{b}_y + \langle w\rangle'\overline{b}_z = 0, \quad (12)$$

where continuity in the cross-bank/vertical plane has been invoked. In the balance expressed by equation (12), tidal period fluctuations in buoyancy result from advection of the mean buoyancy gradients by the dominant tidal velocities. With the tidal excursion ($\sim$7 km) only slightly smaller than frontal/topographic scales ($\sim$10 km), the neglect of the nonlinearities in equation (11) on the Northern Flank is not a priori justifiable. We note, however, from Figure 7 that the horizontal velocity-buoyancy product, $\langle v\rangle'\langle b\rangle'$, varies most strongly at the quarter-diurnal period, whereas the buoyancy itself exhibits semi-diurnal dominance. At the M_2 period, the root-mean-square value over the entire cross-section of $(\langle v\rangle'\langle b\rangle' - \overline{\langle v\rangle'\langle b\rangle'})_y$ is a factor of 3 smaller than the corresponding rms value of $\langle v\rangle'\overline{b}_y$, indicating the approximate validity of equation (12). We therefore proceed with equation (12), as do *Loder and Horne* [1991], in order to obtain analytical expressions for the skew flux, which can be evaluated using the observations. We subsequently will demonstrate, using the gridded phase-mean series, that the error in the computed skew flux associated with the neglect of the tidal products in equation (11) is relatively small compared with other sources of error.

[40] For an oscillatory velocity field given by $\langle v\rangle' = v_0 cos(\omega t + \phi_v)$ and $\langle w\rangle' = w_0 cos(\omega t + \phi_w)$, following *Loder and Horne* [1991], the cross-bank and vertical buoyancy skew flux components are

$$(F_{s2}, F_{s3}) = \left(\overline{\langle v\rangle'\langle b\rangle'}, \overline{\langle w\rangle'\langle b\rangle'}\right) = \left(D_1\overline{b}_z, -D_1\overline{b}_y\right) \quad (13)$$

where the subscripts (1, 2, 3) denote the (x, y, z) directions and D_1, the x component of the skew diffusivity, is given by

$$D_1 = \frac{-w_0 v_0}{2\omega} sin(\phi_w - \phi_v). \quad (14)$$

We focus on the x component of the skew diffusivity vector because the assumption of negligible along-bank property gradients implies zero cross-bank and vertical skew fluxes arising from the other skew diffusivity components. As *Loder and Horne* [1991] point out, there is a large along-bank (x) skew flux arising from the rotary nature of the horizontal tidal currents combined with cross-bank property gradients. We ignore this component because we are interested in cross-bank fluxes and because the along-bank uniformity assumption is consistent with a nondivergent x component flux.

[41] The evaluation of the skew diffusivity given by equation (14) requires knowledge of the tidal period vertical velocity field, which we estimate from the data in two independent ways. At each cross-bank grid point, an M_2 harmonic is fit to the phase mean series of cross-bank velocity and buoyancy (e.g., Figures 7a and 7b). The first method uses these harmonic coefficients with estimates of the mean buoyancy gradients to solve equation (12) for the amplitude and phase of the vertical velocity. We limit application of this procedure to those cross-bank grid points where the harmonic fits explain at least 25% of the buoyancy variance. An alternate method utilizes the cross-bank continuity equation with the assumption of zero vertical velocity at the surface. Integration from the surface to depth z with $w(0) = 0$ gives

$$w(z) = \int_z^0 v_y \, dz. \quad (15)$$

We evaluate equation (15) using the v harmonic constants, approximating derivatives using centered differences and integrals with the trapezoidal formula.

[42] Estimates of the errors in the least-squares determined harmonic coefficients are made using standard tech-

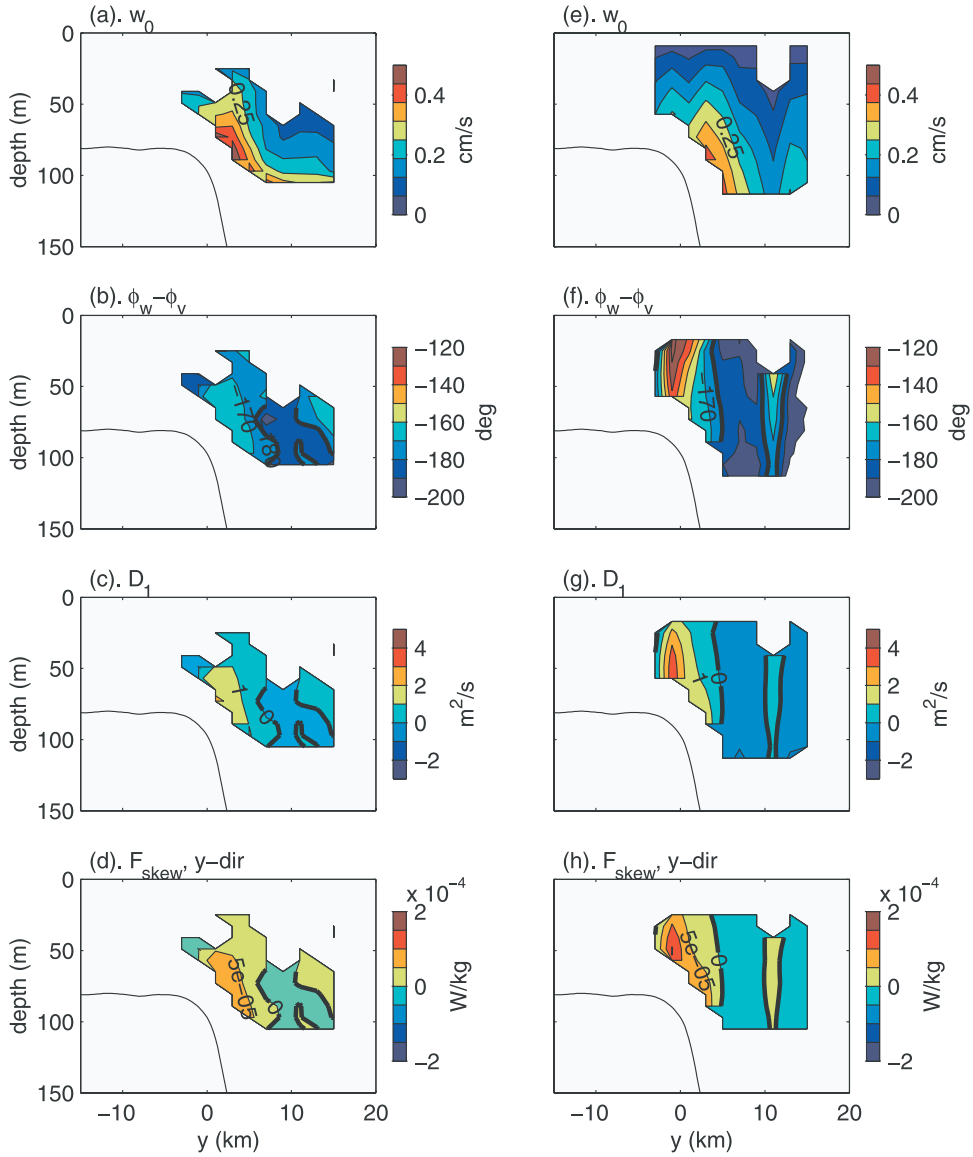

Figure 9. Estimates of vertical velocity, skew diffusivity, and cross-bank skew flux derived from (left) the tidal buoyancy balance and (right) continuity. The fields are shown only at locations where the vertical velocity amplitude is larger than its standard error. (a, e) Vertical velocity amplitude. (b, f) Vertical velocity phase relative to off-bank velocity. (c, g) Skew diffusivity. (d, h) Skew flux. The heavy contour in Figures 9b and 9f is −180, and in Figures 9c, 9d, 9g, and 9h is the 0 contour.

niques [*Press et al.*, 1992]. These uncertainties are propagated through the various computations described above, in order to derive estimates for the standard errors in the vertical and Stokes velocities, and skew fluxes.

[43] Vertical velocities estimated using the two methods (Figure 9) display similar patterns in the region of the bank edge. In Figure 9, the fields are masked where the vertical velocity amplitude does not exceed its associated standard error. Amplitudes increase rapidly toward the bottom with maximum values of ∼0.5 cm/s occurring just north of the bank edge (Figures 9a and 9e). The phase estimates (Figures 9b and 9f) in this region ($\langle w \rangle'$ lags $\langle v \rangle'$ by 160–180°) indicate that the motion in the *y-z* plane is indeed rotary (counterclockwise). Moving on-bank from the edge, the vertical velocity from the second method lags $\langle v \rangle'$ by a larger amount (120–140°), indicating that the tidal velocity vector is more highly rotary there. The diagnosed vertical velocity field is used with equation (14) to estimate the skew diffusivity allowing the skew fluxes to be calculated using equation (13). The cross-bank skew flux estimated using both methods (Figures 9d and 9h) is of the same sign (off-bank) and exhibits a similar bottom intensification over the bank edge as the observed tidal pumping flux (Figure 6). The near-bottom peak in skew flux calculated using continuity-derived $\langle w \rangle'$ occurs slightly farther on-bank, corresponding to the increased rotary nature of the estimated velocity field there. Skew flux magnitudes are generally somewhat lower than observed fluxes over the bank edge, possibly due to the neglect of nonlinearity in the skew flux model.

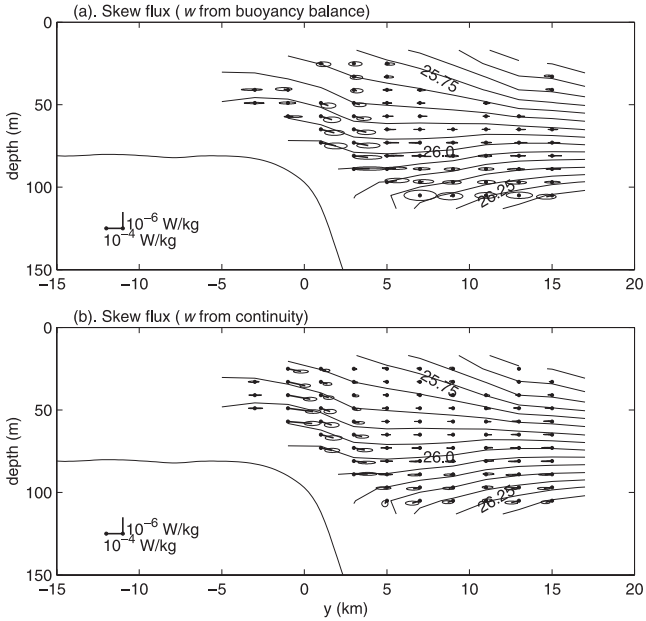

Figure 10. Estimated skew flux vectors superimposed on the mean σ_t field for the case of (a) vertical velocity estimated from tidal period buoyancy balance and (b) vertical velocity estimated from continuity. The standard errors for the estimated fluxes are shown as ellipses centered at the flux vector tips.

[44] As expected, because isopycnals are not flat, there is a vertical skew flux component as well. This is shown in Figure 10, where the skew fluxes in the y–z plane are plotted as a vector field overlaying the mean σ_t section. The flux vectors are oriented along the mean isopycnals. The standard errors for the estimated flux components, shown as ellipses about the flux vector tips, are quite large in places. The largest flux vectors above the bank edge are significantly off-bank, however, and the general agreement of the two methods leads us to believe that at least the qualitative pattern is correct.

[45] The standard errors in skew fluxes shown in Figure 10 arise from uncertainties in the harmonic constituents that are due to sampling inadequacy, nonstationarity of the time series, and the collapse of the data to two dimensions. As noted above, the linearization of the buoyancy balance leading to the analytical form for the skew flux requires neglect of terms which although small, may not be entirely negligible. The error associated with this approximation is essentially an inadequacy of the skew flux model. We can crudely estimate the magnitude of this model error by adding to equation (12) an error term $E = (\langle v\rangle' \langle b\rangle' - \overline{\langle v\rangle' \langle b\rangle'})_y$, which can be evaluated from the observations. It can be shown that inclusion of this error term results in a correction to the cross-isobath skew flux (F_{s2}) of $\Delta F_{s2} = \frac{E_0 v_0}{2\omega} sin(\phi_E - \phi_v)$, where E_0 and ϕ_E are the M_2 amplitude and phase of the error term. Over the cross-section, the rms value of this correction term is 1×10^{-5} W/kg. This is small compared with the rms value of the cross-isobath skew flux standard error of 5×10^{-5} W/kg for method 1, and 3×10^{-5} W/kg for method 2, suggesting that the linearization is not a serious source of error.

7. Stokes Velocity

[46] As shown by *Middleton and Loder* [1989], the skew flux can be partitioned into two components, one of which is nondivergent and thus does not impact scalar evolution. This component is purely an artifact of the Eulerian nature of the eddy flux calculation, as illustrated by the example in Figure 8. For oscillatory motion that is steady in time, the divergent component of the skew flux is [*Middleton and Loder*, 1989]

$$(F_{sd2}, F_{sd3}) = (v^s \overline{b}, w^s \overline{b}), \tag{16}$$

where the (nondivergent) Stokes velocity (v^s, w^s) is related to spatial gradients of the skew diffusivity by

$$(v^s, w^s) = (-D_{1z}, D_{1y}). \tag{17}$$

The divergence of the skew flux then arises from the advection of the mean scalar gradient by the Stokes velocity [*Middleton and Loder*, 1989],

$$\nabla F_s = v^s \overline{b}_y + w^s \overline{b}_z. \tag{18}$$

[47] The Stokes velocity field inferred from equation (17), shown in Figure 11, is subject to large errors that preclude the explicit calculation of the skew flux divergence. Nonetheless, there are qualitative features evident in Figure 11 that merit discussion. The estimated errors are somewhat

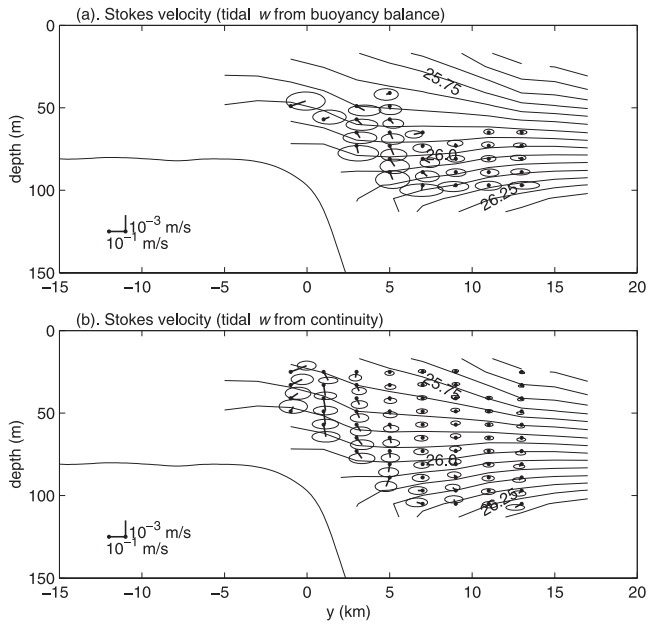

Figure 11. Estimated Stokes velocity vectors superimposed on the mean σ_t field for the case of (a) vertical velocity estimated from tidal period buoyancy balance and (b) vertical velocity estimated from continuity. The standard errors for the estimated velocities are shown as ellipses centered at the velocity vector tips.

smaller using $\langle w \rangle'$ from continuity, making the Stokes velocity field in Figure 11b somewhat more robust than that of Figure 11a, although we note again the qualitative similarity of fields derived from the two independent methods. There is a downward Stokes velocity in the zone $0 < y < 5$ with largest values of $w^s = -0.08 \mp 0.03$ cm/s, and the suggestion of upward flow for $y < 0$. The sign of the horizontal Stokes velocity is uncertain due to the large error magnitudes.

[48] Estimated Stokes velocities are in places directed up or down the mean buoyancy gradient (Figure 11), which from equation (18) implies a non-zero skew flux divergence. The skew flux divergence can be qualitatively assessed by examination of Figure 11 with reference to equation (18). Locations where the velocity vector points toward (away from) denser water are characterized by a convergence (divergence) in skew buoyancy flux resulting in a tendency of increasing (decreasing) buoyancy with time. The region $y > 0$ is thus a region of convergence with buoyant water being forced downwards, while in the region $y < 0$ there is the suggestion of a flux divergence with dense water upwelling.

8. Discussion

[49] The vertical turbulent diffusivities ($1 \times 10^{-3} - 1 \times 10^{-1}$ m^2/s) inferred from analysis of overturns are generally somewhat higher than previous estimates on the Northern Flank of Georges Bank from microstructure observations [*Horne et al.*, 1996; *Yoshida and Oakey*, 1996] and dye dispersion [*Houghton and Ho*, 2001]. This may arise partly because the CTD pressure resolution and sampling rate impose limits on the smallest detectable overturns, resulting in a bias towards large Thorpe scales (and diffusivities). This being said, however, we have no reason to doubt the spatial structure of vertical mixing exhibited in Figure 5. Although turbulent diffusivity is highest over the bank, the lack of significant vertical stratification there results in low buoyancy flux. Highest vertical turbulent buoyancy fluxes arise when stratification and high diffusivities coexist. On the Northern Flank in early spring, this occurs near the bottom at the bank edge at roughly the mean position of the front separating bank water from deep Maine Bottom Water.

[50] The spatial pattern of the cross-isobath skew flux due to M_2 tidal motion, estimated using two independent methods, is similar to that of the tidal pumping flux computed from the covariance of the phase-mean series of buoyancy and cross-bank velocity. This suggests that the estimated tidal pumping flux is predominantly the cross-isobath component of the skew flux resulting from rotary tidal motion in the $y - z$ plane. Because the mean isopycnals near bottom in the vicinity of the bank edge slope down to the north, the tidal pumping flux appears to be countergradient.

[51] *Ou et al.* [2000] studied a simple model for tidally-induced heat fluxes in which the presence of vertical mixing alters the relative phasing of velocity and temperature such that a tidal pumping flux arises. As this frictional mechanism has been shown by *Ou et al.* [2000] to produce locally countergradient property fluxes, it is useful to evaluate this theory for the region of the bank edge. Using a vertical eddy diffusivity of 1×10^{-2} m^2/s (a bank-edge value from Figure 5) in 100-m water depth, the dimensionless diffusivity ($\kappa = K_\rho/(\omega H^2)$) of *Ou et al.* [2000] for M_2 periods is $\sim 7 \times 10^{-3}$. For this diffusivity, the *Ou et al.* [2000] model (their Figure 3) predicts a maximum nondimensional down-gradient flux of 0.05 at a nondimensional depth of about 0.7 and a slightly smaller counter-gradient flux in the lower 10% of the water column (a region that is not covered by our observations). Using tidal velocity (0.5 m/s) and buoyancy fluctuation (1×10^{-3} m/s^2) scales from Figure 7 gives a dimensional flux of $\sim 2.5 \times 10^{-5}$ W/kg at a depth below the surface of 70 m (the location of the peak tidal pumping flux in Figure 6). This is roughly a factor of 2–4 smaller than the observed fluxes (see Figure 6). More importantly, however, the predicted flux in the portion of the water column covered by our observations is down-gradient, whereas the observed flux is up-gradient. Thus we conclude that the observed tidal pumping flux is not likely due to a frictional mechanism, but is more likely an advective effect.

[52] The tidal period vertical velocities (Figure 9) that produce the rotary motion responsible for the skew flux appear to be the signature of an internal tide. The vertical velocity phase propagation (not shown) is upward and off-bank. The associated group velocity would be downward and also off-bank suggesting a generation region near the break in slope at the bank edge consistent with the estimate of *Marsden* [1986] (see also *Dale et al.* [2003] for a discussion of the internal tide). At the generation site the near-bottom vertical velocity is expected to be exactly 180° out of phase with the cross-bank velocity. The vertical velocity relative phase estimates in Figures 9b and 9f do not, however, extend close enough to the bottom to verify this, although they do not rule it out.

[53] As shown by *Middleton and Loder* [1989], the skew flux can be partitioned into nondivergent and divergent components, with the former not impacting the evolution of scalar concentration fields. The divergence of the skew flux is the scalar product of the Stokes velocity and mean concentration gradient [*Middleton and Loder*, 1989]. The Stokes velocity fields estimated here (Figure 11) exhibit downward flow in the interior of the water column for $y > 0$ with a suggestion of upwelling occurring at $y < 0$. Although the calculated horizontal Stokes velocities are not statistically significant, there is a suggestion in Figure 11 of a clockwise gyre that is consistent with the results of dye release experiments [*Houghton and Ho*, 2001] and numerical model-based particle tracking experiments [*Chen and Beardsley*, 1998]. *Houghton and Ho* [2001] observed the on-bank movement of a near-bottom dye patch on the Northern Flank with subsequent vertical mixing and off-bank advection of dye at mid-depth. Particles released near the Northern Flank edge in the model experiments of *Chen and Beardsley* [1998] executed elliptical residual trajectories such that the near-bottom flow was on-bank and upward and the flow 20–30 m above bottom was off-bank and downward. Although strictly speaking we should compare the diagnosed Lagrangian mean velocity with the particle trajectories of *Chen and Beardsley* [1998], in fact the mean Eulerian currents are weak compared to Stokes velocities making the latter an adequate proxy for the Lagrangian current field.

[54] The possible upwelling region just on-bank from the bank edge ($y < 0$) is the area in which mean isopycnals are domed upward (see Figure 11 and several individual cross-

bank sections of *Dale et al.* [2003]), suggesting an advective origin for this feature. A similar doming of isopleths of a passive tracer (with source in the deep bottom water) was also found by *Chen and Beardsley* [1998], both with and without tracer diffusion, further suggesting that this feature results primarily from advection.

9. Conclusions

[55] Hydrographic and velocity measurements along with overturn-derived vertical mixing estimates from a 50 by 50 km region on the Northern Flank of Georges Bank have been collapsed into a two-dimensional (cross-bank, vertical) coordinate system and analyzed to determine the spatial structure of property fluxes in the vicinity of a front. Vertical turbulent buoyancy fluxes peak near the bottom at the bank edge and decrease toward the center of the bank as the water column becomes more well-mixed and away from the bank because strong stratification inhibits mixing there. Computed horizontal buoyancy flux is dominated by the tidal pumping contribution resulting from correlation between cross-bank velocity and buoyancy tidal-period fluctuations.

[56] The tidal pumping flux appears to be the horizontal component of a skew flux directed along the mean isopycnals. Because the skew flux has a (nondivergent) component arising from the Eulerian nature of the measurements, one cannot use this flux to predict the evolution of property fields. Isolating the nondivergent component of the skew flux provides the Stokes velocity field, which in the present case is essentially the Lagrangian velocity. The computed Stokes velocity is downward to the north of the bank edge and upward just on-bank, suggesting the presence of a closed gyre consisting of off-bank Stokes velocity at mid-depth and on-bank flow near the bottom. This is consistent with the observations of *Houghton and Ho* [2001] and model results of *Chen and Beardsley* [1998] and suggests the existence of a mechanism whereby nutrients and biological organisms in deep Maine Bottom Water may be pumped upward and onto the Northern Flank of Georges Bank.

[57] **Acknowledgments.** We thank Marc Willis and Linda Fayler, OSU Marine Technicians, who were responsible for the success of the SeaSoar observations. We also thank the officers and crew of R/V *Oceanus* for their help in making the continuous SeaSoar operations possible. Postprocessing of the SeaSoar data was performed by Robert O'Malley (OSU). Sandra Fontana (URI) carried out the processing of the ADCP data. The material in this paper is based upon work supported by the National Science Foundation under grants OCE9806650 and OCE9813641 and is contribution 379 of the U.S. GLOBEC program.

References

Barth, J. A., S. D. Pierce, and R. L. Smith, A separating coastal upwelling jet at Cape Blanco, Oregon and its connection to the California Current System, *Deep Sea Res., Part II*, *47*, 783–810, 2000.

Brown, W. S., and J. A. Moody, Tides, in *Georges Bank*, edited by R. H. Backus, pp. 100–107, MIT Press, Cambridge, Mass., 1987.

Burgett, R. L., D. Hebert, and N. S. Oakey, The vertical structure of turbulence on the southern flank of Georges Bank, *J. Geophys. Res.*, *106*, 22,545–22,558, 2001.

Chen, C., and R. C. Beardsley, Tidal mixing and cross-frontal particle exchange over a finite amplitude asymmetric bank: A model study with application to Georges Bank, *J. Mar. Res.*, *56*, 1163–1201, 1998.

Dale, A. C., D. Ullman, J. A. Barth, and D. Hebert, The front on the Northern Flank of Georges Bank in spring: 1.Tidal and subtidal variability, *J. Geophys. Res.*, *108*(CXX), doi:10.1029/2002JC001327, in press, 2003.

Dillon, T. M., Vertical overturns: A comparison of Thorpe and Ozmidov length scales, *J. Geophys. Res.*, *87*, 9601–9613, 1982.

Flagg, C. N., Hydrographic structure and variability, in *Georges Bank*, edited by R. H. Backus, pp. 108–124, MIT Press, Cambridge, Mass., 1987.

Galbraith, P. S., and D. E. Kelley, Identifying overturns in CTD profiles, *J. Atmos. Oceanic Technol.*, *13*, 688–702, 1996.

Garrett, C. J. R., and J. W. Loder, Dynamical aspects of shallow sea fronts, *Philos. Trans. R. Soc. London, Ser. A*, *302*, 563–581, 1981.

Garrett, C. J. R., J. R. Keeley, and D. A. Greenberg, Tidal mixing versus thermal stratification in the Bay of Fundy and Gulf of Maine, *Atmos. Ocean*, *16*, 403–423, 1978.

Gregg, M. C., Diapycnal mixing in the thermocline: A review, *J. Geophys. Res.*, *92*, 5249–5286, 1987.

Horne, E. P. W., J. W. Loder, W. G. Harrison, R. Mohn, M. R. Lewis, B. Irwin, and T. Platt, Nitrate supply and demand at the Georges Bank tidal front, in *Topics in Marine Biology*, edited by J. D. Ros, Sci. Mar., *53*, 145–158, 1989.

Horne, E. P. W., J. W. Loder, C. E. Naimie, and N. S. Oakey, Turbulence dissipation rates and nitrate supply in the upper water column on Georges Bank, *Deep Sea Res., Part II*, *43*, 1683–1712, 1996.

Houghton, R. W., and C. Ho, Diapycnal flow through the Georges Bank tidal front: A dye tracer study, *Geophys. Res. Lett.*, *28*, 33–36, 2001.

Loder, J. W., and E. P. W. Horne, Skew eddy fluxes as signatures of nonlinear tidal current interactions, with application to Georges Bank, *Atmos. Ocean*, *29*, 517–546, 1991.

Marsden, R. F., The internal tide on Georges Bank, *J. Mar. Res.*, *44*, 35–50, 1986.

Middleton, J. F., and J. W. Loder, Skew fluxes in polarized wave fields, *J. Phys. Oceanogr.*, *19*, 68–76, 1989.

Osborn, T. R., Estimates of the local rate of vertical diffusion from dissipation measurements, *J. Phys. Oceanogr.*, *10*, 83–89, 1980.

Ou, H.-W., C.-M. Dong, and D. Chen, On the tide-induced property flux: Can it be locally countergradient?, *J. Phys. Oceanogr.*, *30*, 1472–1477, 2000.

Peters, H., and R. Bokhorst, Microstructure observations of turbulent mixing in a partially mixed estuary: II., Salt flux and stress, *J. Phys. Oceanogr.*, *31*, 1105–1119, 2001.

Press, W. H., S. A. Teukolsky, W. T. Vetterling, and B. P. Flannery, *Numerical Recipes in FORTRAN: The Art of Scientific Computing*, 2nd ed., Cambridge Univ. Press, New York, 1992.

Schumann, U., and T. Gerz, Turbulent mixing in stably stratified shear flows, *J. Appl. Meteorol.*, *34*, 33–48, 1995.

Smyth, W. D., J. N. Moum, and D. R. Caldwell, The efficiency of mixing in turbulent patches: Inferences from direct simulations and microstructure observations, *J. Phys. Oceanogr.*, *31*, 1969–1992, 2001.

Thorpe, S. A., Turbulence and mixing in a Scottish Loch, *Philos. Trans. R. Soc. London, Ser. A*, *286*, 125–181, 1977.

Thorpe, S. A., On the shape and breaking of finite amplitude internal gravity waves in a shear flow, *J. Fluid Mech.*, *85*, 7–31, 1978.

Townsend, D. W., and A. C. Thomas, Winter-spring transition of phytoplankton chlorophyll and inorganic nutrients on Georges Bank, *Deep Sea Res., Part II*, *48*, 199–214, 2001.

Yoshida, J., and N. S. Oakey, Characterization of vertical mixing at a tidal-front on Georges Bank, *Deep Sea Res., Part II*, *43*, 1713–1744, 1996.

J. A. Barth and A. C. Dale, College of Oceanic and Atmospheric Sciences, Oregon State University, 104 Ocean Administration Building, Corvallis, OR 97331-5503, USA. (barth@coas.oregonstate.edu; acd@coas.oregonstate.edu)

D. Hebert and D. S. Ullman, Graduate School of Oceanography, University of Rhode Island, 215 South Ferry Road, Narragansett, RI 02882, USA. (dhebert@gso.uri.edu; d.ullman@gso.uri.edu)